Hierarchical refinement of primary phases in a multicomponent Al-14Si-CuNiMg casting alloy by ultrasonic melt treatment

Min-Su Jo [a,b], Young-Hee Cho [a,*], Jung-Moo Lee [a], Soo-Bae Kim [a], Jun-Yun Kang [a], Jae-Gil Jung [a], Jae-il Jang [b]

[a] Division of Metallic Materials, Korea Institute of Materials Science, Changwon 51508, Republic of Korea
[b] Division of Materials Science and Engineering, Hanyang University, Seoul 04763, Republic of Korea

A R T I C L E   I N F O

A B S T R A C T

The combined effects of ultrasonic melt treatment (UST) with the cooling rate on the microstructural evolution in a multicomponent Al-14Si-CuNiMg casting alloy was investigated. UST was applied to a melt at 800°C, followed by casting into a steel step mold at cooling rates in the range of 4-32 K/s. UST in the fully liquid state significantly reduced the sizes of the primary phases (the phases formed before Al) crystallized in the initial stage of solidification, and the structural refinement by UST became more pronounced for a faster cooling. With trace additions of Ti, V and Zr, the primary phase is most likely $(Al,Si)_3(Zr,Ni,Fe)$, and primary Si and then Al_3Ni are sequentially formed upon solidification. AlP particles, well-known nucleants for primary Si, were also found to exist inside the $(Al,Si)_3(Zr,Ni,Fe)$ and Al_3Ni which exhibited a very low lattice misfit with AlP (~0.7 and 4.7%, respectively). This importantly suggests that AlP can nucleate all the primary phases while it has the highest efficiency of structural refinement by UST for $(Al,Si)_3(Zr,Ni,Fe)$ phase that first nucleated in the molten metal. The nucleation of the primary phases was quantified using an analytical model based on exponential statistics. The hierarchical refinement operated by UST is further discussed.

1. Introduction

Multicomponent Al-Si casting alloys have been widely used to manufacture machine parts and high-temperature powertrains because they provide important features, including light weight, good wear resistance, excellent castability and low thermal expansion coefficient. In order to operate the alloys at increasingly higher temperatures, alloy design for the Al-Si casting alloys has been approached with the addition of substantial amounts of transition metals (TMs such as Cu, Ni, Co, Ti/V/Zr) to form thermally stable intermetallic phases [1–7]. Ni has been reported to be effective for producing stable aluminides such as Al_3Ni and Al_9FeNi in the presence of Fe. More recently, we have found that the combined addition of Zr with Ni can also form a new $(Al,Si)_3(Zr,Ni,Fe)$ phase in the early stage of nucleation [8]. It has been reported that the interconnectivity of the thermally stable phases (e.g. TMs-rich intermetallic phases, primary Si, etc.) as well as their volume fractions can affect the high temperature strength [9]. For a well-connected multiphase networks, increasing the hard phases while maintaining the morphologies with a rather high aspect ratio can be required. Such intermetallic phases are likely to form a massive acicular

morphology during solidification, which may deteriorate the mechanical properties of the alloys. In this regard, the structural refinement of constituent phases has been extensively attempted either by adding chemical modifiers [10] or employing special casting processes such as rapid solidification, melt thermal-rate treatment [11–13], and ultrasonic melt treatment (UST) [14–16]. Among them, UST is often considered as one of the most efficient methods because it can achieve not only the microstructural refinement but also the improved quality of the casting products [17–20].

UST involves two important phenomena; acoustic cavitation and streaming. Applying UST in the fully liquid state can affect both nucleation [14,21,22] and growth of the primary crystalline phases [23] upon solidification. Ultrasound-induced acoustic cavitation in a melt can generate a localized hot spot with temperature and pressure up to ~5000°C and ~500 atmosphere, respectively, when the cavitation bubbles collapsed [24]. This intensive heat and pressure would increase the surface reactions [25] and thus enhance the wettability of non-wetting nucleating particles in the Al alloy melt [14,21,26,27]. Additionally, the high pressure by bubble collapse can elevate the melting point of a melt, following the Clapeyron equation [28], which has an effect of increase in undercooling for nucleation. Bubble expansion during cavitation is also

Table 1
Chemical composition of the multicomponent Al-14Si casting alloy.

Element	Si	Cu	Ni	Mg	Fe	Mn	Ti	V	Zr	P	Al
[wt.%]	14.61	3.00	4.50	0.52	0.40	0.19	0.11	0.09	0.19	0.0035	bal.

suggested to induce undercooling at the bubble surface, promoting the nucleation event [29].

It has been confirmed by transmission electron microscopy (TEM) studies that UST activated non-wetting particles (e.g. Al_2O_3, $MgAl_2O_4$) to directly nucleate the primary phases such as primary Si, α-Al, Al_3Ti, Al_3Zr and $Al_3(Ti,Zr)$ [14,21,22,26]. The studies have also revealed that the nucleation event in the presence of UST is also strongly dependent on lattice misfit, the number and size of nucleants, and undercooling [21]. Therefore, the cavitation-induced activation of the nucleants along with their improved dispersion by acoustic streaming could result in ultrasonic refinement, if sufficient undercooling for nucleation is provided [14,21,22,26]. This is further supported by the fact that ultrasonically induced refinement became more pronounced when the cooling rate was increased [14,18].

In hypereutectic Al-Si alloys, the primary phase is most likely primary Si and is often found to form onto AlP which is always present even at a quite low level of phosphorous (e.g., on the order of 10 ppm). Jung et al. [14] observed that AlP formed on $MgAl_2O_4$ (which are well wetted and were thoroughly dispersed by UST) can effectively nucleate primary Si in a hypereutectic Al-18Si alloy. Nevertheless, Si phases are likely to form in a relatively coarse manner in the Al-18Si alloy and were not effectively refined by UST at a low cooling rate of 2 K/s [14]. Such a high Si content also increases the melting point of the alloy, resulting in lower castability. For the new Al-Si piston alloy development, therefore, the authors lowered the Si level to 12-14 wt.% while increasing the content of transition metals (TMs) for the high temperature strength, which would be equivalent with that of the Al-18Si alloy.

In commercial Al-Si piston alloys designed for high-temperature applications, however, the primarily crystallized phase is no longer primary Si but is more likely TM-bearing intermetallic phases, since the alloys contain a substantial amount of Ni with trace Ti, V and Zr. We recently discovered the nucleation of a new $(Al,Si)_3(Zr,Ni,Fe)$ intermetallic phase on AlP prior to primary Si [8], which would certainly affect the subsequent primary Si nucleation and the resulting structural refinement, particularly when employing UST. In fact, primary Si was not notably refined by UST, which could be possibly related to the nucleation event of the primary phases, sharing the common nucleation sites of AlP among all the primary phases. Nevertheless, there is still a lack of understanding about ultrasonic refinement performance in a multicomponent Al-Si casting alloy where a complex solidification sequence exists in the initial stage. In the new Al-14Si casting alloy (mainly containing Cu and Ni with trace additions of Ti, V and Zr) we designed recently [8], a few silicides and the Zr-rich phase, $(Al,Si)_3(Zr,Ni,Fe)$ were found to firstly form in the molten metal, followed by the crystallization of primary Si and Al_3Ni when increasing Ni content in excess of Cu amount. However, the formation of such primary phases in a multicomponent system is somewhat serial, occurring within narrow temperature intervals. Hence, the refinement of the primary phases with UST should be approached with a comprehensive understanding of the nucleation behavior of each phase.

In view of this, the present investigation was carried out to clearly understand the microstructural evolution in the early stage of solidification of the multicomponent Al-14Si casting alloy, while structural refinement was attempted through UST combined with various cooling rates. With a systematic study on the nucleation event of each primary intermetallic phases, we aimed to quantitatively evaluate the effect of UST on the refinement performance of all the primary phases. The role of AlP and its interaction with UST is further discussed to clarify the refinement mechanism observed in this work.

2. Experimental

The examined Al-14Si alloy was produced in a foundry facility of Dong Yang Piston Co., Ltd. (Ansan, Korea), and its chemical composition is given in Table 1. Approximately 500 kg of the alloy was melted in an an electric resistance furnace, and the melt was degassed with inert gas (Ar), then isothermally held at 800°C. 2.5 kg of the molten metal was transferred to a steel ladle where UST was applied using a ceramic horn (sialon) at a temperature from 800 to approximately 770°C. UST was performed in the liquid state at a resonant frequency of 20 kHz and electric power of 325 W using a piezoelectric transducer for 20 s while the melt was cooled in air. After UST, the melt was immediately cast into a steel step mould (preheated to 230°C) at various cooling rates of 4-32 K/s. The step mould was designed with dimensions of 200 × 240 mm. The thickness of two die halves were 45 mm, and it contained four steps of cavity thicknesses, 40, 20, 10, 4 mm.

For comparison, alloy "without UST" was prepared by placing a melt weighing 2.5 kg in the steel ladle, followed by pouring into the same step mould. T7 heat treatment (solid solution treatment at 470°C for 2 h followed by aging at 230°C for 5 h) was carried out on the cast alloys.

Metallographic samples were prepared by standard polishing procedure, with a final polishing by a 0.05 μm colloidal silica suspension. The microstructures of the specimens were observed using a Nikon MA200 optical microscopy (OM) and a JEOL JSM-6610LV scanning electron microscopy (SEM) equipped with an energy dispersive X-ray spectrometer (EDS). Morphological characteristics and volume fractions of the constituent phases were analysed on 3 × 3 mosaic images (200x) with a field size of around 1.8 × 1.4 mm² using an image analyser (I-solution DT). Electron backscatter diffraction (EBSD) combined with EDS was also applied to identify intermetallic phases using a JEOL JSM-7900F field emission SEM (FE-SEM) and AZtecSynergy software. A thin foil sample containing phases of interest was prepared using a JEOL JIB-4601F focused ion beam (FIB), and then analyzed with a JEOL JEM-2100F TEM.

3. Results

3.1. Characterization of the primary phases

Fig. 1(a) shows a typical back-scattered electron (BSE) image exhibiting the intermetallic phases solidified at a cooling rate of 4 K/s in the alloy without UST. Considering the Scheil simulation for the early stage of solidification using Thermo-Calc with a TCAL3 database (Fig. 1(b)), it was predicted that a few silicides (e.g., Si_2Ti, Si_2Zr) could form first, and then large quantities of primary Si and Al_3Ni (12.4 and 8.5 mass%, respectively) formed at 610-617°C [30]. However, as evidenced in Fig. 1(a), the observed Ni-rich phases in the alloy were not Al_3Ni but Al_9FeNi and $Al_3(Cu,Ni)_2$. Note that coarse plate-like $(Al,Si)_3(Zr,Ni,Fe)$ intermetallic phase was often found to form with a few tens of μm size, and were experimentally confirmed to nucleate onto AlP at ~630°C, even prior to the formation of primary Si [8]. The combined use of FactSage with a FTlite database [31] for the thermodynamic calculations enabled the prediction of AlP formation at trace additions of 35 ppm P. As illustrated in Fig. 1(b), AlP is expected to form at ~668°C and could pre-exist in the melt in the early stage of solidification.

Identification of the primary phases in the alloy without UST was performed using a combination of EBSD and EDS, as exhibited in Fig. 2. The typical compositions of the various intermetallic phases observed in the alloy were first quantified by EDS and the potential candidates corresponding to each phase were then deduced using the crystallog-
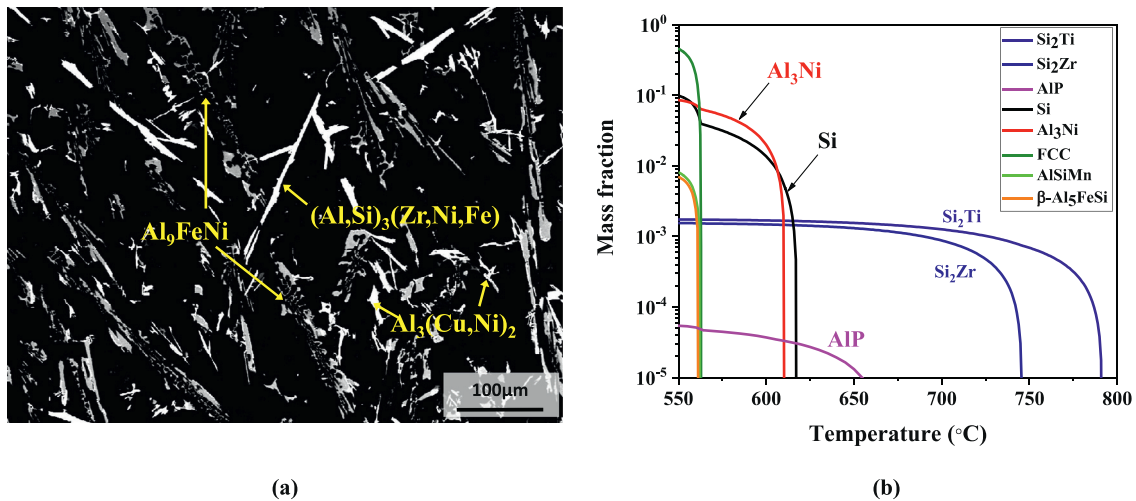
(a)   **(b)**

Fig. 1. (a) BSE image showing typical intermetallic phases observed in the T7 treated alloy without UST, solidified at a cooling rate of 4 K/s and (b) Scheil simulation predicting the phases formed in the early stage of solidification of the Al-14Si casting alloy, using Themo-Calc with the TCAL3 database and FactSage with FTlite database [8,30,31].
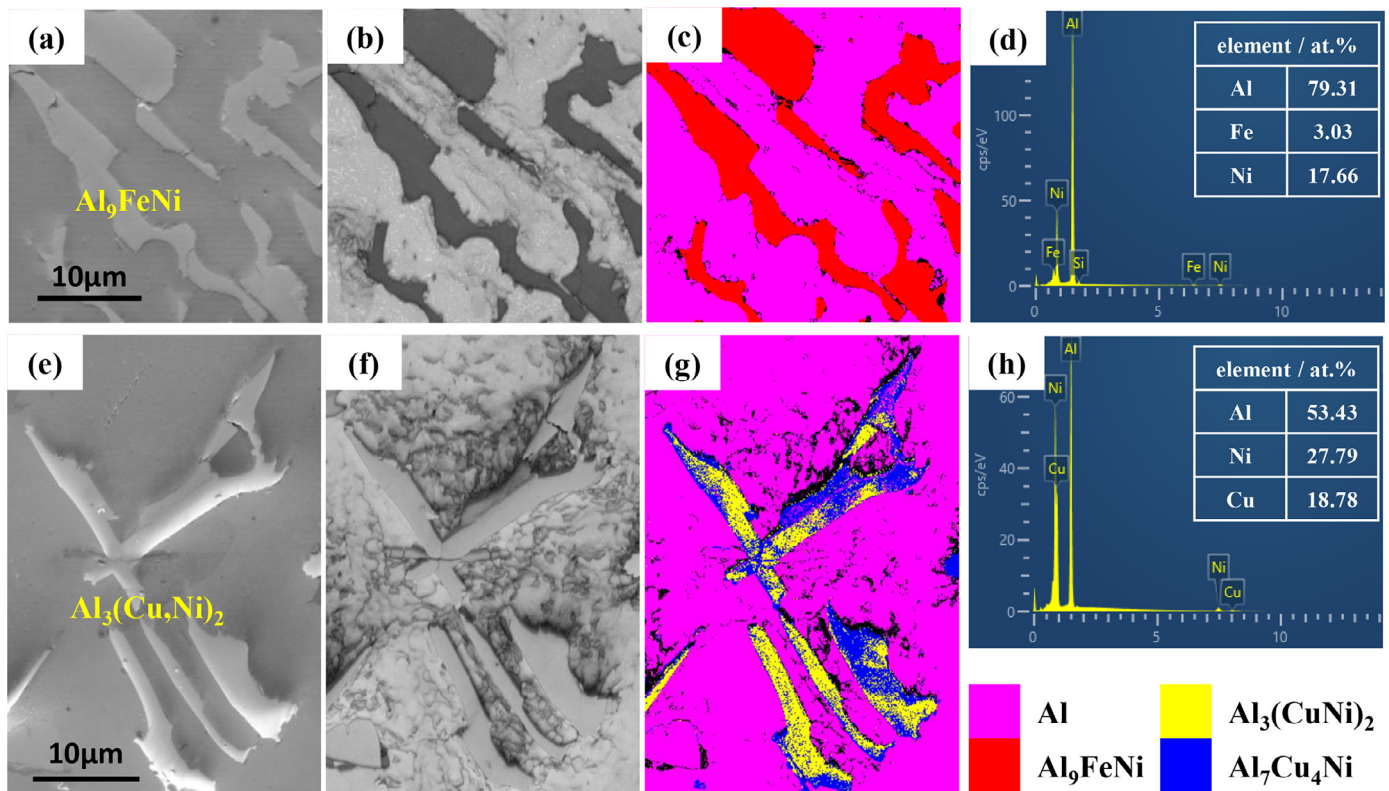

Fig. 2. SEM images showing (a) Al_9FeNi and (e) $Al_3(Cu,Ni)_2$ intermetallic phases formed in the T7 treated alloy and their corresponding (b, f) EBSD band contrast maps, (c, g) EBSD phase maps and (d, h) EDS spectra, respectively. EBSD phase maps in (g) show that the $Al_3(Cu,Ni)_2$ is surrounded by a layer of Cu-rich Al_7Cu_4Ni intermetallics, indicating that Cu diffusion occurring during solidification can induce the transformation of primary Al_3Ni intermetallics into $Al_3(Cu,Ni)_2$ as well as Al_7Cu_4Ni.

raphy information as listed in Table 2 [8,32]. The existence of Ni-rich intermetallic phases, either Al_9FeNi or $Al_3(Cu,Ni)_2$, was further confirmed by EBSD phase maps (see Fig. 2(c) and (g)). Al_9FeNi phase, which exhibits a fishbone morphology with a maximum length of a few hundred μm, as shown in Fig. 1(a), contains a high Ni content with a key element of Fe (Fig. 2(d)). In the thermodynamic calculation in Fig. 1(b), β-Al_5FeSi phase was expected, but Al_9FeNi was found to formed due to a high content of Ni. In the multicomponent Al-12Si piston alloys containing low Fe, thermodynamic calculations predicts

that Al_9FeNi is most likely to form after the Al-Si eutectic reaction at 550-560 °C instead of the formation of the β-Al_5FeSi phase [1]. The EBSD phase map analysis in Fig. 2(g) confirms that Al_9FeNi phase is isomorphous with monoclinic Al_9Co_2 phase. Interestingly, $Al_3(Cu,Ni)_2$ phase is partially surrounded by a thin layer of a rather Cu-rich Al_7Cu_4Ni intermetallic phase formed along the $Al_3(Cu,Ni)_2$/Al interface (see Fig. 2(g)).

Considering additional solubility for different elements in each intermetallic phase, this suggests that Cu diffusion upon solidification

Table 2
Properties of the primary phases observed in the alloys investigated [8,32].

| Phase	Composition (at. %)					Crystallographic data [8,32]				
	Al	Si	Fe	Ni	etc.	Crystal structure	Space group	Lattice parameter	Closely packed orientation	Lattice misfit with AlP (%)
AlP	n/a	–	–	–	**P** n/a	cubic	$F\bar{4}3m$ (216)	a = b = c = 5.451 Å	(111)[1$\bar{1}$0]	–
(Al,Si)3(Zr,Ni,Fe)	50.9–51.1	16.5–18.4	1.7–2.6	21.9–22.8	**Zr** 4.7–5.1	tetragonal	I4/mmm (139)	a = b = 4.005 Å c = 15.475 Å	(100)[001] (100)[010]	0.7 4.3
Al9FeNi	80.9–84.2	–	1.3–3.2	13.6–16.5	–	monoclinic	$P2_1/c$ (14)	a = 6.290 Å b = 6.210 Å c = 8.560 Å β = 94.76 °	(001)[010]	18.4
Al3Ni	n/a	–	–	n/a	–	orthorhombic	Pnma (62)	a = 6.598 Å b = 7.352 Å c = 4.802 Å	(001)[010]	4.7
Al3(Cu,Ni)2	62.8–74.9	–	–	13.5–21.3	**Cu** 11.3–19.7	hexagonal	$p\bar{3}m1$ (164)	a = b = 4.028 Å c = 4.891 Å γ = 120 °	(001)[100]	n/a
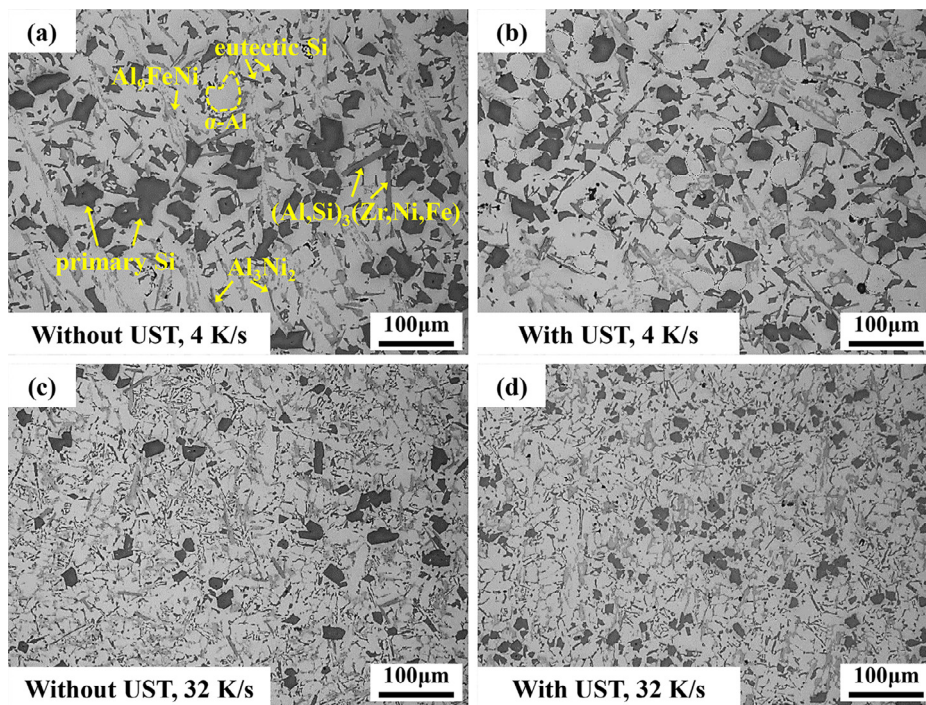
Fig. 3. Optical micrographs showing the microstructures of the T7 treated alloys solidified at cooling rates of (a, b) 4 K/sec and (c, d) 32 K/sec: (a, c) without UST and (b, d) with UST.

could induce the transformation of primary Al_3Ni intermetallics into $Al_3(Cu,Ni)_2$ as well as Al_7Cu_4Ni [1,33,34].

3.2. UST induced structural refinement

Fig. 3 shows optical micrographs of the T7 treated Al-14Si alloys without and with UST for two different cooling rates of 4 and 32 K/s. In both alloys, the average size of the constituent phases becomes smaller for higher cooling rate. In the absence of UTS, the alloy solidified at 4 K/s mainly consisted of α-Al, primary Si, eutectic Si and intermetallic phases such as $(Al,Si)_3(Zr,Ni,Fe)$, Al_9FeNi and $Al_3(Cu,Ni)_2$ as shown in Fig. 3(a). While more uniform distributions of the constituent phases were achieved by UST at both cooling rates (see Figs. 3(b) and 3(d)), UST-assisted refinement of primary Si became more pronounced at a higher cooling rate (32 K/s). The BSE images in Fig. 4 confirms that the UST induced not only notable refinement of $(Al,Si)_3(Zr,Ni,Fe)$ phase

but significant change in its morphology from plate-like to a more compact form (see the insets of Fig. 4 showing 3D morphology of the phase in the deep etched samples). As with the primary Si, UST combined with a fast cooling resulted in a marked reduction in the size of the $(Al,Si)_3(Zr,Ni,Fe)$, as evidenced in Fig. 4(d).

The sizes of primary Si and $(Al,Si)_3(Zr,Ni,Fe)$ were quantitatively measured and are summarized in Figs 5. While UST has a strong refining effect in both primary Si and $(Al,Si)_3(Zr,Ni,Fe)$, the refining effect appears to be more prominent for $(Al,Si)_3(Zr,Ni,Fe)$ compared to primary Si. In Fig. 5(a), the average size of primary Si was slightly reduced (45.4 to 39.4 μm) by UST for 4 K/s, whereas for 32K/s, the overall size distribution of primary Si in the alloy with UST shifted further towards a smaller size (mostly in the range of 24-34 μm). In Fig. 5(b), the size distributions of $(Al,Si)_3(Zr,Ni,Fe)$ are broader for 4 K/s, while the average size is significantly reduced by UST (from 73.4 to 44.5 μm). More interestingly, combining UST with fast cooling led to the most dra-
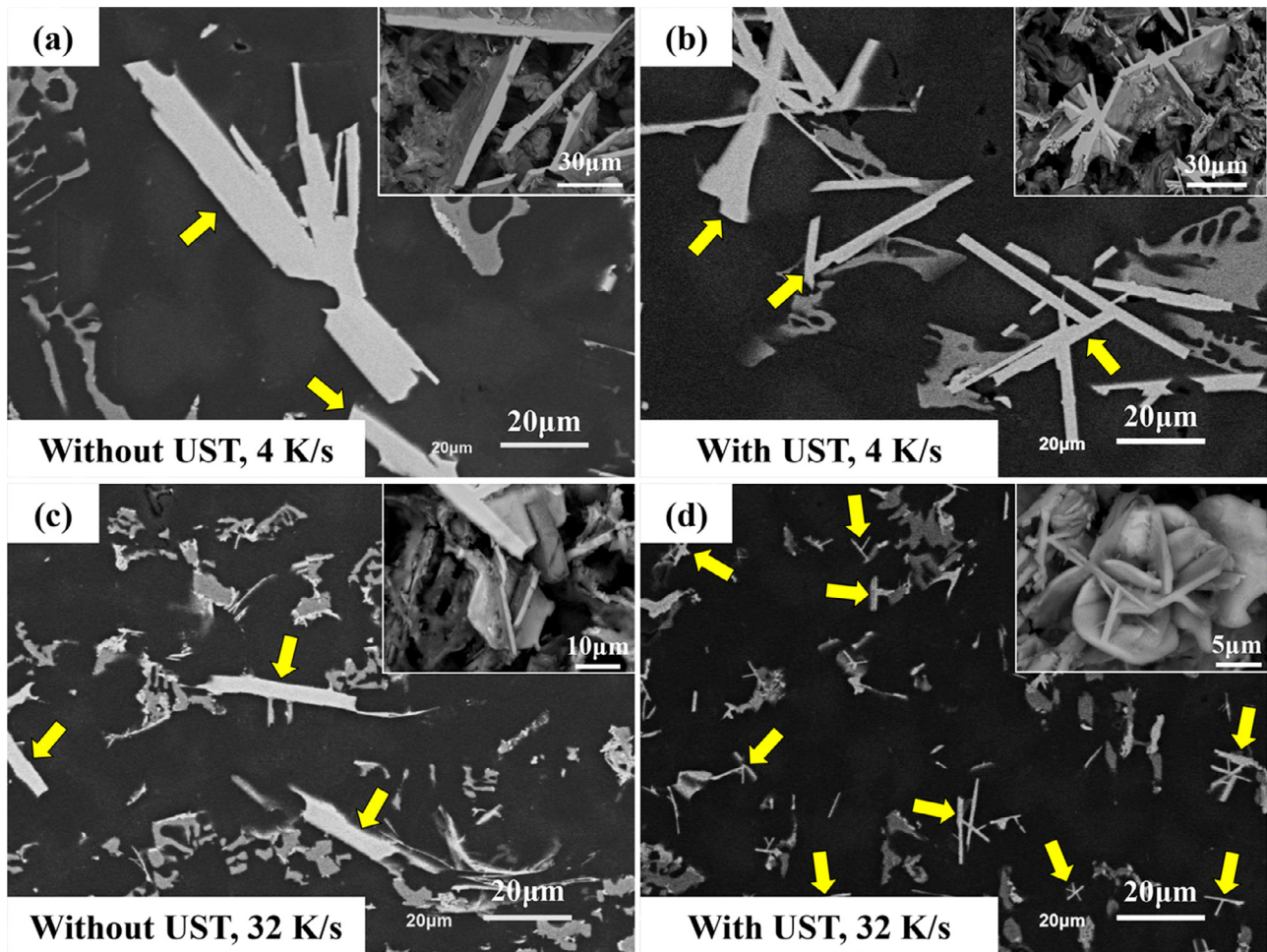
Fig. 4. BSE images showing $(Al,Si)_3(Zr,Ni,Fe)$ intermetallic phases formed in the T7 treated alloys solidified at cooling rates of (a, b) 4 K/sec and (c, d) 32 K/sec: (a, c) without UST and (b, d) with UST. Each inset image of the deep etched samples respectively exhibit the 3D morphology of the $(Al,Si)_3(Zr,Ni,Fe)$ phases, which vary with UST and cooling rate.
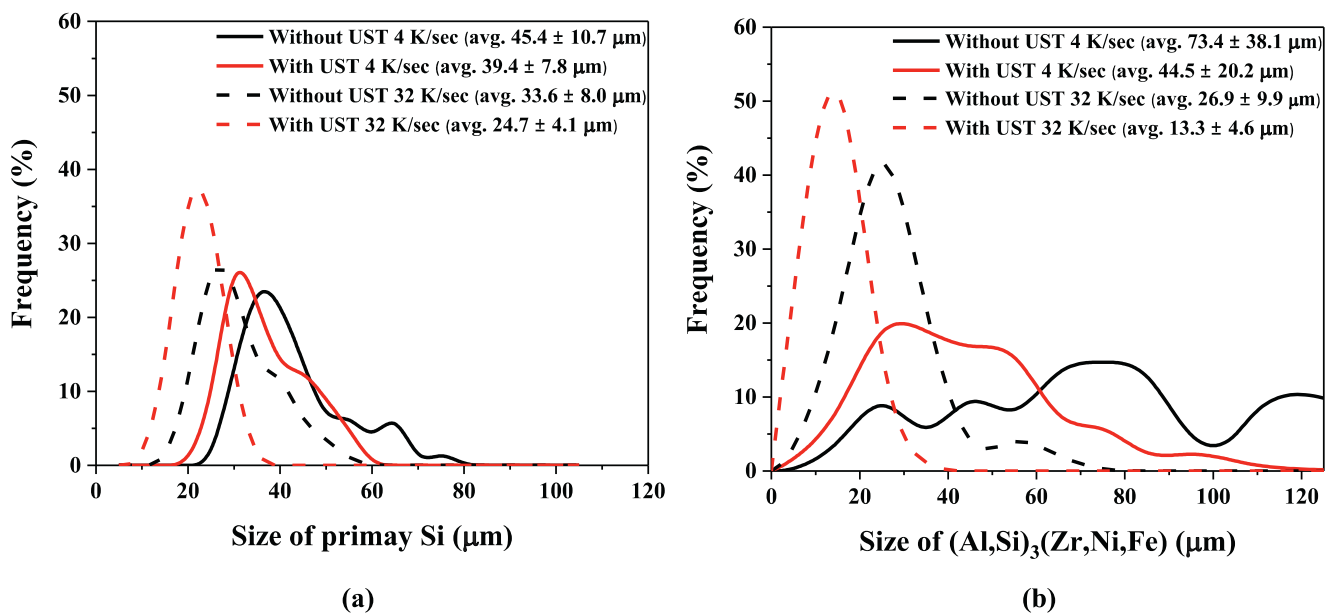

Fig. 5. The effect of UST and cooling rate on the size distribution of the (a) primary Si and (b) $(Al,Si)_3(Zr,Ni,Fe)$ phase in the T7 treated alloys.
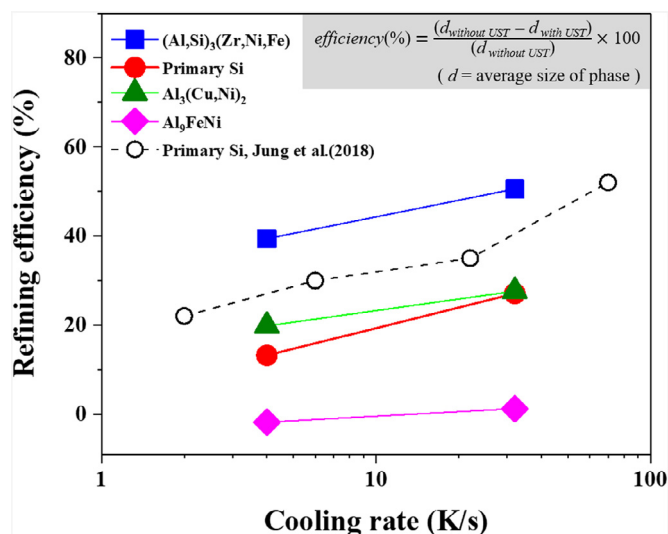
Fig. 6. The variation in the refining efficiency of the constituent phases by UST as a function of cooling rate.

matic structural refinement of $(Al,Si)_3(Zr,Ni,Fe)$, reducing the average size down to 13.3 μm.

The UST's refining efficiency (that can be determined as the UST-induced size change divided by the original size) for each phase was plotted as a function of the cooling rate in Fig. 6. For all the phases investigated, the refining efficiency of UST was enhanced by increasing the cooling rate and became the best for $(Al,Si)_3(Zr,Ni,Fe)$; that is, 39 and 51 % for 4 and 32 K/s, respectively, which are much higher than those achieved for primary Si (13-27%). An interesting feature in Fig. 6 is that the refining efficiency for primary Si is lower in the present Al-14Si piston alloy than in the Al-18Si piston alloy in Ref. [14]. This is probably due to the difference in solidification sequence as well as availability of nuclei particles. Knowing that both primary Si and $(Al,Si)_3(Zr,Ni,Fe)$ phases nucleate on AlP in the Al-14Si alloy, preoccupying AlP particles with the first crystallized $(Al,Si)_3(Zr,Ni,Fe)$ can reduce the available number of nuclei for primary Si in the Al-14Si alloy. In the Al-18Si alloy, on the other hand, only primary Si is most likely to form first onto AlP during solidification. Hence, the ultrasonically enhanced heterogeneous nucleation could preferentially promote the nucleation event of primary Si in the Al-18Si alloy, yielding the high refining efficiency of 22-52% in the cooling rate range of 2-70 K/s [14] (see Fig. 6). A more detailed discussion on the role of the AlP particle as a nucleating particle is further quantitatively approached in Section 4.1.

A quantitative analysis of the sizes of other Ni-rich Al_9FeNi and $Al_3(Cu,Ni)_2$ phases was also carried out. As shown in electronic Supplementary Figs. S1(a) and (b), the lower cooling rate of 4 K/s likely allows Al_9FeNi intermetallics to grow as large as 250-300 μm in both alloys with and without UST. Even under fast cooling (32 K/s), which reduces the overall size of the Al_9FeNi, structural refinement by UST was not observed; i.e., the average size is almost the same (65-66 μm) for both alloys (see electronic Supplementary Figs. S1(c) and (d)), confirming the negligible refining efficiency for Al_9FeNi in Fig. 6. $Al_3(Cu,Ni)_2$ phase (which may originate from primary Al_3Ni) exhibits a significant refinement by UST for both 4 and 32 K/s. A precise image analysis revealed that the average size of the $Al_3(Cu,Ni)_2$ intermetallics was reduced from 33 to 26 and 19 to 14 μm at 4 and 32 K/s, respectively (electronic Supplementary Fig. S2). In Fig. 6, the estimated refining efficiency for $Al_3(Cu,Ni)_2$ increased from 20 to 28% with the cooling rate from 4 to 32 K/s, which is similar to those of primary Si.

3.3. Nucleating potency of AlP for primary phases

AlP (cubic, $F\bar{4}3m$, a = 5.451 Å) is well known as the most potent nuclei for primary Si [35]. In the present Al-14Si alloy containing 35

ppm P, AlP was found to nucleate $(Al,Si)_3(Zr,Ni,Fe)$ along with primary Si [8]. As elaborated above, the ultrasonic structural refinement is certainly associated with the heterogeneous nucleation. The evidence that the refining efficiency depends on solidification sequence suggests primary phases' sharing common nucleation sites of AlP.

It is therefore of interest to investigate the role of AlP in nucleating all the primary phases (i.e., $(Al,Si)_3(Zr,Ni,Fe)$, primary Si, Al_3Ni and Al_9FeNi) by evaluating the degree of the lattice mismatch at the solid/substrate interface. The interfacial energy at the nucleating substrate is generally accepted to be an intrinsic factor controlling the nucleation event of the solid phase, and nucleation potency is higher for a better matching. From this viewpoint, we preliminarily assessed the lattice misfit between AlP and the primary phases, as listed in Table 2. While primary Si and $(Al,Si)_3(Zr,Ni,Fe)$ had a small mismatch with AlP (0.2 and 0.7%, respectively), the estimated lattice misfits of Al_3Ni and Al_9FeNi with AlP were 4.3 and 18.4%. The calculated atomic mismatch values along the close-packed directions were small and less than the suggested 10% maximum [36] for all the primary phases except for Al_9FeNi. Hence it is reasonable to expect that AlP phase can act as potential nuclei for all the primary phases but Al_9FeNi.

Fig. 7(a) exhibits a SEM micrograph showing $Al_3(Cu,Ni)_2$ phase where an internal particle was often entrapped. The dashed line across the $Al_3(Cu,Ni)_2$ with the internal particle was further analyzed by EDS. The EDS line scan results in Fig. 7(b) confirm the presence of Al and P within the particle, suggesting that AlP particle can act as a nucleation site for $Al_3(Cu,Ni)_2$. To clarify the crystallographic information of $Al_3(Cu,Ni)_2$ and AlP, we extracted a TEM sample containing the $Al_3(Cu,Ni)_2$ phase and AlP particle through FIB milling. Cross-sectioning across the dashed line in Fig. 7(a), we extracted a thin foil sample for the TEM analysis. Fig. 7(c) shows a TEM image of an $Al_3(Cu,Ni)_2$ phase containing an internal particle well-wetted in the alloy with UST (for 4 K/s). Elemental mapping on of the area of interest (squared in Fig. 7(c)) by EDS revealed that the internal particle mainly consists of Al, P and O as shown in Fig. 7(d) and is most probably AlP. The presence of O in large quantities could be due to a strong oxidation tendency of AlP. From a high-resolution TEM (HR TEM) image in Fig. 7(e), it is also evident that $Al_3(Cu,Ni)_2$ phase has an intimate physical relationship with AlP, exhibiting a coherent or semi-coherent interface between the $Al_3(Cu,Ni)_2$ and AlP. However, it is very difficult to identify the diffraction patterns obtained from AlP due to the oxidation, which disturbed the determination of the orientation relationship between the phases. Nevertheless, it is suggested that primary Al_3Ni could possibly nucleate on AlP in the early stage of solidification, and then the subsequent Cu diffusion into Al_3Ni during solidification leads to the transformation into the $Al_3(Cu,Ni)_2$ as observed in Figs. 2(e) to 2(h).

Fig. 8 illustrates the atomic configurations of Al_3Ni and AlP in their respective closely packed planes with closely packed rows. From their crystal structures, the most closely directions are $[010]_{Al_3Ni}$ on the most closely packed $(001)_{Al_3Ni}$ plane and $[1\bar{1}0]_{AlP}$ on the $(111)_{AlP}$ plane. The atomic mismatch between the two closely packed directions was calculated to be 4.7 %, indicating that AlP can be also being a potential nucleation site for primary Al_3Ni.

4. Discussion

As observed in Section 3.2, the efficiency of the ultrasonically induced structural refinement was the highest for $(Al,Si)_3(Zr,Ni,Fe)$ amongst all the primary phases in the Al-14Si alloy whereas it is less significant for primary Si and Al_3Ni (or $Al_3(Cu,Ni)_2$). This is probably because nucleation occurs on a common nucleation site in AlP. If the hypothesis that AlP nucleates all the primary phases is correct, then we can conjecture whether or not the hierarchical refinement performance by UST was simply caused by the absolute lack of AlP nuclei. To address this, we explored the vital role of AlP in the UST-induced hierarchical refinement by precisely quantifying the numbers and size of AlP nu-
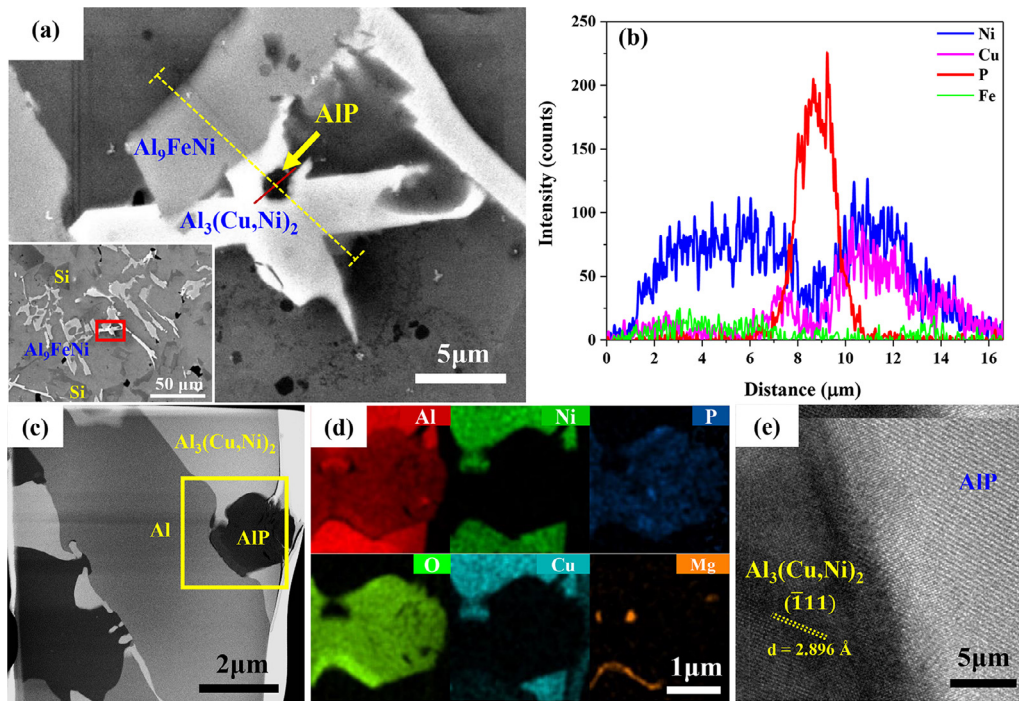
Fig. 7. SEM image showing (a) an $Al_3(Cu,Ni)_2$ phase and the existence of an internal AlP particle within the $Al_3(Cu,Ni)_2$ phase in the T7 treated alloy. (b) EDS line scan across the phases containing the internal particle in (a) showing the presence of P and O. (c) TEM image showing the $Al_3(Cu,Ni)_2$ intermetallic phase adjacent to the AlP particle and (d) EDS maps for (c) the square marked area, exhibiting the distribution of constituent elements. (e) HR TEM image showing the interface between the $Al_3(Cu,Ni)_2$ / AlP phases.
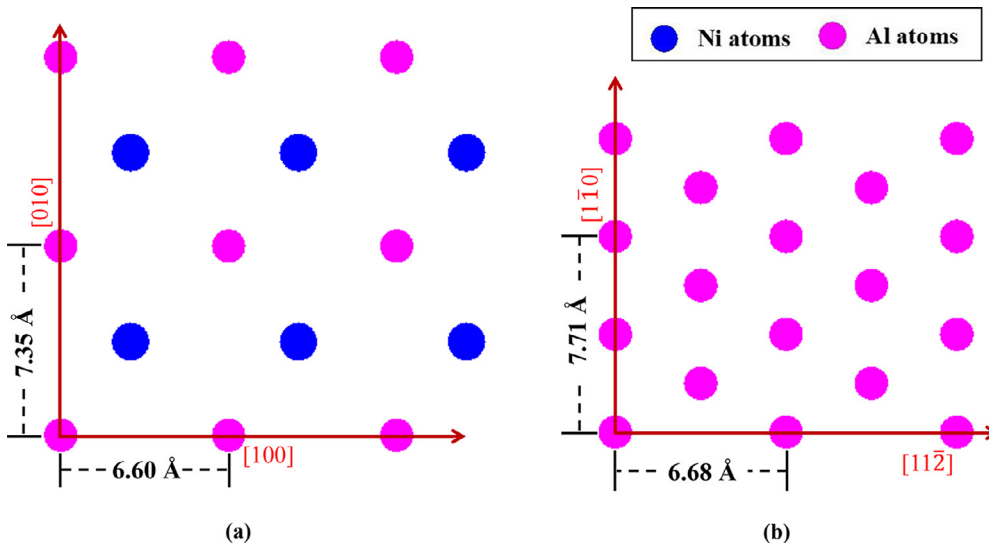

Fig. 8. Atomic distributions on the closely packed planes of (a) (001) for Al_3Ni with an orthorhombic structure (atoms with 10% offset from (001)) and (b) (111) for AlP with a cubic structure.

clei available in both alloys with and without UST for the two different cooling rates.

4.1. Quantitative analysis of nucleation

Statistical approaches are attractive since they can simply quantify the size distribution of various inoculant particles whose measurement is difficult and experimentally somewhat tricky [21,37–39]. Various probability density distribution models have been attempted, including log-normal [38], exponential [21,37], and Weibull distribution [39]. In the present study, AlP nucleant particles were frequently found within the primary phases (i.e., $(Al,Si)_3(Zr,Ni,Fe)$, Al_3Ni (or $Al_3(Cu,Ni)_2$) and primary Si), although its strong nature of oxidation limits the measurement

of real size. Moreover, the amount of P added to the alloy is very low (~35 ppm) and thus the distribution of particle size using common metallographic examination is likely less reliable.

Recently, Jung et al. [14] employed a pressure filtration testing method to collect inoculant particles from Al melt and thereby determined the AlP size distribution through image analysis. The observed distribution of AlP could be well fitted by a log-normal one [14]. However, the number of the particles having very small size (< 200 nm) can be misinterpreted since some scratches and other surface defects could be counted as particles during image analysis [39]. If the measured numbers of this small particles are erroneous and thus can be neglected, the distribution of the particles would follow an exponential distribution [14,21,37,39]. Therefore, in this work, an exponential dis-

Table 3

Measured undercoolings and the number density of primary phases nucleated in the alloys with and without UST. Nucleation parameters are also obtained by fitting of Eq. (3).

| | Cooling rate (K/s) | ΔT_m (K) | Number of active nucleation site, N_v (m^{-3}) | | AlP total number, N_{tot} (m^{-3}) | Mean diameter of AlP particles, d_a (μm) | Critical diameter of AlP nucleant particle, d^* (μm) |
			Measured	Calculated			
Without UST	4	0.9	2.44×10^{12}	1.97×10^{12}	8.59×10^{12}	2.04	2.58
	9	1.7	4.37×10^{12}	3.94×10^{12}			1.37
	32	5.6	7.04×10^{12}	6.57×10^{12}			0.41
With UST	4	1.5	8.53×10^{12}	8.61×10^{12}	5.37×10^{13}	0.86	1.56
	9	2	1.41×10^{13}	1.36×10^{13}			1.17
	32	6.1	3.40×10^{13}	3.44×10^{13}			0.38

tribution model was employed to estimate the size distribution of AlP particles using the following probability density function

$$f(d) = \lambda \exp(-\lambda d) \qquad (1)$$

where d is the particle diameter and λ is a distribution parameter given as $1/d_a$ (d_a: mean particle diameter).

It is known that a crystal initially forms on a potent nucleant particle (here, AlP) in a melt at very low undercooling and then grows by reducing the curvature radius of its interface with the melt to a critical radius, r^*. Free growth of the crystal from the particle is then possible when the diameter of the particle, $d \geq r^*$ [37]. The critical diameter of the nucleant particle, d^* where the free growth of the nucleus proceeds, can be derived from the classical expression for critical nucleus size;

$$d^* \geq \frac{4\sigma}{\Delta S \Delta T_m} \qquad (2)$$

where ΔT_m is undercooling for nucleation, σ is the solid-liquid interfacial energy and ΔS is the entropy of fusion per unit volume [37]. Eq. (2) indicates that a smaller nucleant particle requires greater undercooling for their active nucleation and free growth. From Eqs. (1) and (2), the number of active nucleation sites, N_v is given by

$$N_v = N_{tot} \exp\left(-\frac{b}{\Delta T_m}\right) \qquad (3)$$

where N_{tot} is the total number of nucleant particles available for nucleation and b is the nucleation parameter given by

$$b = \frac{4\sigma}{\Delta S d_a} \qquad (4)$$

Due to the lack of relevant data (e.g., average site size, density of substrates, wetting angle θ) in the present state of knowledge, the magnitudes of N_{tot} and b were estimated from experimental results. N_v was estimated by counting the number densities of the primary phases nucleating by AlP (N_v) and undercooling (ΔT_m) was determined by analyzing cooling curves achieved for the alloys with and without UST for different cooling rates, as listed in Table 3. The ΔT_m is the maximum undercooling for nucleation, that is, $\Delta T_m = T_e - T_m$ where T_e is the equilibrium temperature (liquid temperature) of the Al-14Si alloys with and without UST and T_m is the minimum temperature prior to recalescence. In this work, the T_e and T_m for the alloys in this study were obtained from the reaction of primary Si (see electronic Supplementary Figs. S4 and S5). This is due to the fact that the other primary phases having little fraction made it difficult to accurately detect T_e and T_m from cooling curves achieved at different cooling rates. The T_e was analyzed on a cooling curve with a very slow cooling rate of 0.8-0.9 K/s in order to decide the nucleation temperature of primary Si in both the alloys with and without UST (Supplementary Fig. S4(a)). The T_m of primary Si was determined by analyzing the cooling curve at each cooling rate of 4, 9, and 32 K/s for the alloys with and without UST. Then the nucleation parameters can be fitted to a logarithmic form, yielding a linear plot between $\ln N_v$ and $1/T_m$ as shown in Fig. 9(a). The determined values of N_{tot} and b from the plots are also listed in Table 3.

It is noteworthy that only particles having size greater than 2.58 and 1.56 μm can be active in the alloy without UST and with UST, respectively (for 4 K/s). Using the total number of estimated particles, N_{tot}, the exponential distributions of all AlP particles present under the different casting conditions can be plotted as a function of the particle diameter by multiplying Eq. (3) by N_{tot}. Fig. 9(b) illustrates the distribution of the total numbers of AlP nucleant particles in the alloys with and without UST. Having obtained the critical size of the nucleant particles for their activation in both alloys with and without UST, the number of activated AlP particles was determined by calculating the shaded areas, as indicated in Fig. 9(b). The results for various cooling rates are listed in Table 3 and are in a good agreement with the measured number density of the primary phases (i.e., N_v in Eq. (3)). It can be also seen in Table 3 that the number of the active nucleation sites increased with cooling rate.

In this study, we have assumed that the size distribution of the AlP nucleant particles existed in the form of an exponential function, while the key parameter values were empirically achieved through Eqs. (3) and (4) by thermal analysis (for ΔT_m) and image analysis (for N_v). Therefore, it is necessary to verify the numerical model by taking the parameters experimentally determined. Provided that AlP particles are cubes with the length dimension of the average AlP diameter, the total volume of AlP particles per 1m^3 of the alloys with and without UST were estimated by multiplying the average AlP volume by N_{tot}. From the theoretical density values of AlP (2.85 g/cm^3) and the Al-14Si alloy (2.81 g/cm^3), the amount of P added to the alloys without UST and with UST can be deduced to be 42 and 76 ppm, respectively. The calculated results are reasonably close to the actual content (~35ppm) added to the both alloys, supporting the validity of the model as well as the relevance of the parameters.

4.2. Mechanism of hierarchical refinement

Based on the quantitative analysis of nucleation in above section, we attempted to find the reason why the refinement efficiency of the primary phases was reduced in the later stage of solidification. As seen in Table 3, the good agreement between the measured and calculated numbers of active nucleation sites (N_v) justifies a hypothesis that AlP particles having size exceeding the critical diameter (d^*) are thoroughly consumed to nucleate the primary phases. Moreover, increasing the cooling rates from 4 to 32 K/s reduced d^* and introduced nearly threefold the number of activated AlP particles, and thereby further promoted the nucleation of the primary phases (see Table 3 and electronic Supplementary Fig. S6). It is well known that the nucleation of a crystal tends to occur on large particles, followed by subsequent nucleation on smaller particles at a greater undercooling, as the melt is cooled below the liquidus temperature [39]. As demonstrated in Section 3.1, the first crystallized phase in the Al-14Si alloy is (Al,Si)$_3$(Zr,Ni,Fe) intermetallic phase that is likely to preferentially consume the activated AlP particles. The following nucleation events of primary Si and Al$_3$Ni (or Al$_3$(Cu,Ni)$_2$) phases are then dependent on the numbers of leftover AlP nuclei available in the very early stage of solidification.
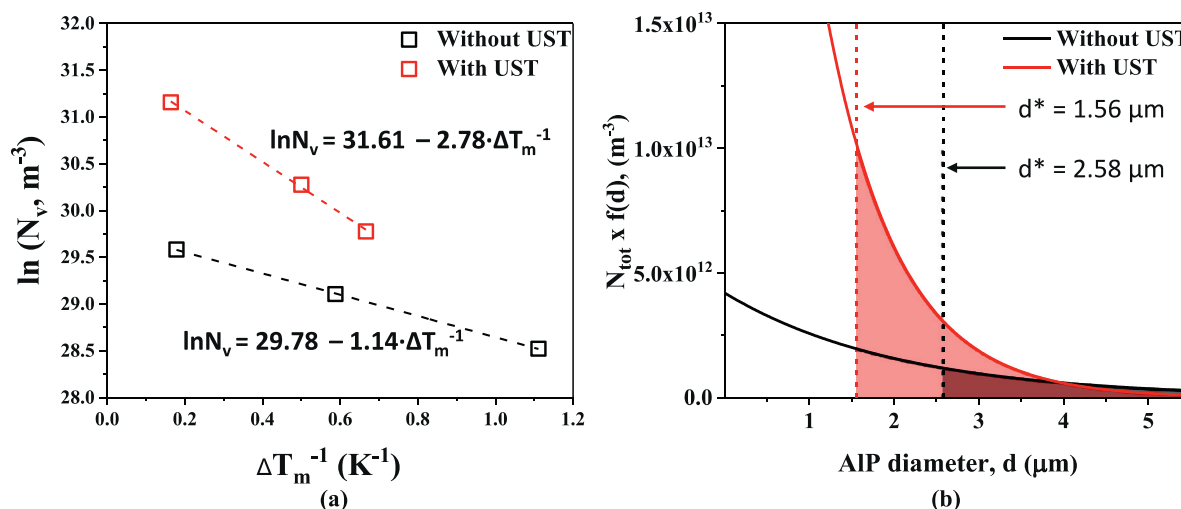
Fig. 9. (a) Linear relationship between the maximum degree of undercooling ΔT_m^{-1} and the volumetric density of the primary phases nucleated in the T7 treated alloys with and without UST. (b) Distribution of the total numbers of AlP nucleants present in the alloys with and without UST as a function of the diameter. The shaded areas under the curve indicates the total number of AlP activated to nucleate the primary phases in the alloys with and without UST, solidified at a cooling rate of 4 K/s.

As evidenced in Figs. 3(a), 3(b) and 5(a), the reduction in refining efficiency of UST for primary Si as well as $Al_3(Cu,Ni)_2$ (for 4 K/s) suggests that the preoccupation of the AlP nucleants by the $(Al,Si)_3(Zr,Ni,Fe)$ would yield less AlP particles available in the melt for the following nucleation (see also electronic Supplementary Fig. S2). However, when the cooling rate increased from 4 to 32 K/s, the number of activated AlP particles increased nearly threefold, which probably introduced sufficient numbers of the nucleants for all the primary phases. Despite the first crystallization of $(Al,Si)_3(Zr,Ni,Fe)$ onto AlP, the remaining AlP particles were still sufficient for the successive nucleation of primary Si and Al_3Ni (or $Al_3(Cu,Ni)_2$) phases at the high cooling rate of 32 K/s. This was further confirmed by evaluating the UST's refining efficiency, of which primary Si and $Al_3(Cu,Ni)_2$ phases increased up to ~30%, as shown in Fig. 6. Considering the fact that all the primary phases nucleate on the common nucleation sites in AlP, we can suggest that the ultrasonic structural refinement is strongly dependent not only on the number of activated AlP particles, but also on the nucleation sequence of the primary phases.

There are three mechanisms suggested for the cavitation induced heterogeneous nucleation [14,19,21,26–29,40]. Among them, both the temperature drop induced by cavitation bubble expansion [29] and the increase in melting point by pressure pulse [28] are unable to clearly explain the UST-induced promotion of nucleation events, as observed in the present study. The refining efficiency for the primary phases, which increased in the order of solidification, could not be simply explained by the temperature change induced by bubble collapse. It is constructive to consider that the prolific number of AlP in the melt with UST vis-à-vis the alloy without UST (see Table 3) is mainly due to their formation on inclusion particles that are well-wetted and better dispersed by cavitation and acoustic streaming. This may also account for the distribution of AlP particles. As estimated in Fig. 9(b), the majority of AlP in the alloys with UST exists as fine (sub-μm-sized) particles, and their number is much larger than in the alloy without UST. Therefore, we could reach the conclusion that the activation of these fine AlP particles is essential for the optimized ultrasonic refinement performance of all the investigated primary phases in the alloy, regardless of the nucleation sequence, and can be achieved by introducing a large undercooling.

5. Conclusions

We investigated the nucleation behavior of each primary phase formed in the Al-14Si-CuNiMg alloy, with and without UST, and so-lidified at various cooling rates of 4-32 K/s. Then we identified the nucleation sites for all the primary phases including $(Al,Si)_3(Zr,Ni,Fe)$, primary Si and Al_3Ni phase, and revealed that the ultrasonic structural refinement of the primary phases is dependent on the nucleation sequence upon solidification.

The combined addition of Zr with Ni to the Al-14Si alloy first induced crystallization of $(Al,Si)_3(Zr,Ni,Fe)$ while primary Si and Al_3Ni phases subsequently nucleated at the beginning of solidification.

Ni-rich intermetallic phases were formed either in the form of Al_3Ni and Al_9FeNi, while Al_3Ni intermetallics were transformed to $Al_3(Cu,Ni)_2$ by Cu diffusion during solidification. Al_9FeNi is unlikely to form in the very early stage of solidification, and grows as large as 250-300 μm at the cooling rate of 4 K/s.

Along with primary Si, AlP particles were also found to nucleate both the $(Al,Si)_3(Zr,Ni,Fe)$ and Al_3Ni intermetallic phases having a very low lattice misfit (0.7 and 4.7%, respectively). However, it appears that Al_9FeNi has a relatively high misfit value of 18.4% with AlP, and is less likely to form on the AlP nucleants.

UST has a refining effect on all the primary phases, $(Al,Si)_3(Zr,Ni,Fe)$, primary Si and Al_3Ni, while exhibiting hierarchical refinement efficiency. The efficiency of the ultrasonically induced structural refinement was the highest for $(Al,Si)_3(Zr,Ni,Fe)$ which crystallized first amongst all the primary phases in the Al-14Si alloy, increasing from 39 to 51 % with the cooling rate from 4 to 32 K/s. However, the refining efficiencies of primary Si and Al_3Ni (or $Al_3(Cu,Ni)_2$) became less significant compared to $(Al,Si)_3(Zr,Ni,Fe)$.

The size distributions of AlP particles in the alloys with and without UST were estimated based on an exponential distribution model, using experimentally determined parameters. UST was found to reduce the average size of AlP from 2.04 to 0.86 μm while significantly increasing the total number of AlP particles from 8.59×10^{12} to 5.37×10^{13}. Knowing that all the primary phases nucleate on the common nucleation sites of AlP, the nucleation sequence as well as the availability of the AlP particles are considered as the key factors influencing the hierarchical refinement performance by UST.

Declaration of Competing Interest

Acknowledgements

Supplementary materials

Supplementary material associated with this article can be found, in the online version, at doi:10.1016/j.mtla.2021.101070.

References

[1] N.A. Belov, D.G. Eskin, N.N. Avxentieva, Constituent phase diagrams of the Al–Cu–Fe–Mg–Ni–Si system and their application to the analysis of aluminium piston alloys, Acta Mater. 53 (17) (2005) 4709–4722.

[2] T. Gao, X. Zhu, Q. Sun, X. Liu, Morphological evolution of ZrAlSi phase and its impact on the elevated-temperature properties of Al–Si piston alloy, J. Alloys Compd. 567 (2013) 82–88.

[3] K.E. Knipling, D.C. Dunand, D.N. Seidman, Precipitation evolution in Al–Zr and Al–Zr–Ti alloys during isothermal aging at 375–425°C, Acta Mater. 56 (1) (2008) 114–127.

[4] Y. Yang, K. Yu, Y. Li, D. Zhao, X. Liu, Evolution of nickel-rich phases in Al–Si–Cu–Ni–Mg piston alloys with different Cu additions, Mater. Des. 33 (2012) 220–225.

[5] Y. Li, Y. Yang, Y. Wu, L. Wang, X. Liu, Quantitative comparison of three Ni-containing phases to the elevated-temperature properties of Al–Si piston alloys, Mater. Sci. Eng. A 527 (26) (2010) 7132–7137.

[6] W. Kasprzak, B.S. Amirkhiz, M. Niewczas, Structure and properties of cast Al–Si based alloy with Zr–V–Ti additions and its evaluation of high temperature performance, J. Alloys Compd. 595 (2014) 67–79.

[7] H.A. Elhadari, H.A. Patel, D.L. Chen, W. Kasprzak, Tensile and fatigue properties of a cast aluminum alloy with Ti, Zr and V additions, Mater. Sci. Eng. A 528 (28) (2011) 8128–8138.

[8] M.-S. Jo, Y.-H. Cho, J.-M. Lee, S.-H. Kim, J.-Y. Kang, J.-G. Jung, S.-B. Kim, J.-i. Jang, A new Zr-rich intermetallic phase in an Al-14Si-3Cu-4.5Ni casting alloy with trace additions of Zr, Intermetallics 117 (2020).

[9] Z. Asghar, G. Requena, H.P. Degischer, P. Cloetens, Three-dimensional study of Ni aluminides in an AlSi12 alloy by means of light optical and synchrotron microtomography, Acta Mater. 57 (14) (2009) 4125–4132.

[10] M.M. Haque, M.A. Maleque, Effect of process variables on structure and properties of aluminium - Silicon piston alloy, J. Mater. Process. Technol. 300 (3-4) (1998) 122–128.

[11] X. Bian, W. Wang, Thermal-rate treatment and structure transformation of Al–13 wt.% Si alloy melt, Mater. Lett. 44 (1) (2000) 54–58.

[12] C.L. Xu, Q.C. Jiang, Morphologies of primary silicon in hypereutectic Al–Si alloys with melt overheating temperature and cooling rate, Mater. Sci. Eng. A 437 (2) (2006) 451–455.

[13] Q. Wang, H. Geng, S. Zhang, H. Jiang, M. Zuo, Effects of melt thermal-rate treatment on Fe-containing phases in hypereutectic Al-Si alloy, Metall. Mater. Trans. A 45 (3) (2014) 1621–1630.

[14] J.-G. Jung, T.-Y. Ahn, Y.-H. Cho, S.-H. Kim, J.-M. Lee, Synergistic effect of ultrasonic melt treatment and fast cooling on the refinement of primary Si in a hypereutectic Al–Si alloy, Acta Mater. 144 (2018) 31–40.

[15] W. Khalifa, Y. Tsunekawa, M. Okumiya, Effect of ultrasonic treatment on the Fe-intermetallic phases in ADC12 die cast alloy, J. Mater. Process. Technol. 210 (15) (2010) 2178–2187.

[16] Y. Zhang, J. Jie, Y. Gao, Y. Lu, T. Li, Effects of ultrasonic treatment on the formation of iron-containing intermetallic compounds in Al-12%Si-2%Fe alloys, Intermetallics 42 (2013) 120–125.

[17] S.-B. Kim, Y.-H. Cho, J.-G. Jung, W.-H. Yoon, Y.-K. Lee, J.-M. Lee, Microstructure-strengthening interrelationship of an ultrasonically treated hypereutectic Al–Si (A390) alloy, Metals Mater. Int. (2018).

[18] S.-B. Kim, Y.-H. Cho, J.-M. Lee, J.-G. Jung, Y.-K. Lee, Combined effects of ultrasonic melt treatment and Cu/Mg solute on the microstructure and mechanical properties of a hypoeutectic Al-7Si Alloy, Metall. Mater. Trans. A 50 (3) (2019) 1534–1544.

[19] G.I. Eskin, Ultrasonic Treatment of Light Alloy Melts, Gordon and Breach Science Publishers, Amsterdam, 1998.

[20] H. Puga, V.H. Carneiro, Light-alloy melt ultrasonication: shorter T6 with higher precipitation strengthening, Metals Mater. Int. (2020).

[21] S.-B. Kim, Y.-H. Cho, M.-S. Jo, J.-G. Jung, Y.-K. Lee, J.-M. Lee, Quantitative approach to realization of ultrasonic grain refinement of Al-7Si-2Cu-1Mg alloy, Sci. Rep. 9 (1) (2019) 17812.

[22] J.-G. Jung, Y.-H. Cho, S.-D. Kim, S.-B. Kim, S.-H. Lee, K. Song, K. Euh, J.-M. Lee, Mechanism of ultrasound-induced microstructure modification in Al–Zr alloys, Acta Mater. 199 (2020) 73–84.

[23] F. Wang, D. Eskin, T. Connolley, J. Mi, Effect of ultrasonic melt treatment on the refinement of primary Al3Ti intermetallic in an Al–0.4Ti alloy, J. Crystal Growth 435 (2016) 24–30.

[24] K.S. Suslick, Sonochemistry, Science 247 (4949) (1990) 1439–1445.

[25] G.I. Eskin, D.G. Eskin, C.R.C. Press, Ultrasonic Treatment of Light Alloy Melts, CRC Press/Taylor & Francis Group, Boca Raton, London; New York, 2017.

[26] F. Wang, D. Eskin, J. Mi, T. Connolley, J. Lindsay, M. Mounib, A refining mechanism of primary Al3Ti intermetallic particles by ultrasonic treatment in the liquid state, Acta Mater. 116 (2016) 354–363.

[27] Y. Han, K. Li, J. Wang, D. Shu, B. Sun, Influence of high-intensity ultrasound on grain refining performance of Al–5Ti–1B master alloy on aluminium, Mater. Sci. Eng. A 405 (1) (2005) 306–312.

[28] J. Hunt, K. Jackson, Nucleation of solid in an undercooled liquid by cavitation, J. Appl. Phys. 37 (1) (1966) 254–257.

[29] O.V. Abramov, Ultrasound in Liquid and Solid Metals, CRC Press, Boca Raton, Florida, 1994.

[30] ThermoCalc-2015a with TCAL3 database. https://www.thermocalc.com, (accessed 14 Augus.2020) 2021.

[31] FactSage with FTlite database. http://www.factsage.com, (accessed 20 August.2020) 2021.

[32] Pearson's Handbook Desk Edition, the second edition ed., ASM International1997 2021.

[33] M. Warmuzek, Chemical composition of the Ni-containing intermetallic phases in the multicomponent Al alloys, J. Alloys Compd. 604 (2014) 245–252.

[34] S.B. Jung, Y. Minamino, T. Yamane, S. Saji, Reaction diffusion and formation of Al3Ni and Al3Ni2 phases in the Al-Ni system, J. Mater. Sci. Lett. 12 (21) (1993) 1684–1686.

[35] C.R. Ho, B. Cantor, Heterogeneous nucleation of solidification of Si in Al-Si and Al-Si-P alloys, Acta Metallurgica et Materialia 43 (8) (1995) 3231–3246.

[36] M.X. Zhang, P.M. Kelly, M. Qian, J.A. Taylor, Crystallography of grain refinement in Mg–Al based alloys, Acta Mater. 53 (11) (2005) 3261–3270.

[37] A.L. Greer, A.M. Bunn, A. Tronche, P.V. Evans, D.J. Bristow, Modelling of inoculation of metallic melts: application to grain refinement of aluminium by Al–Ti–B, Acta Mater. 48 (11) (2000) 2823–2835.

[38] T.E. Quested, A.L. Greer, The effect of the size distribution of inoculant particles on as-cast grain size in aluminium alloys, Acta Mater. 52 (13) (2004) 3859–3868.

[39] E. Fraś, K. Wiencek, M. Górny, H.F. López, E. Olejnik, Equiaxed Grain Count in Aluminum Alloy Castings: Theoretical Background and Experimental Verification, Metall. Mater. Trans. A 44 (13) (2013) 5788–5795.

[40] T.V. Atamanenko, D.G. Eskin, L. Zhang, L. Katgerman, Criteria of grain refinement induced by ultrasonic melt treatment of aluminum alloys containing Zr and Ti, Metall. Mater. Trans. A 41 (8) (2010) 2056–2066.